




In the format provided by the authors and unedited.

Granular aluminium as a superconducting material for high-impedance quantum circuits

Lukas Grünhaupt ^{1,5}, Martin Spiecker^{1,5}, Daria Gusenkova¹, Nataliya Maleeva¹, Sebastian T. Skacel^{1,2}, Ivan Takmakov^{1,2,3}, Francesco Valenti^{1,4}, Patrick Winkel¹, Hannes Rotzinger¹, Wolfgang Wernsdorfer ^{1,2}, Alexey V. Ustinov^{1,3} and Ioan M. Pop ^{1,2*}

¹Physikalisches Institut, Karlsruhe Institute of Technology, Karlsruhe, Germany. ²Institute of Nanotechnology, Karlsruhe Institute of Technology, Eggenstein-Leopoldshafen, Germany. ³Russian Quantum Center, National University of Science and Technology MISIS, Moscow, Russia. ⁴Institute for Data Processing and Electronics, Karlsruhe Institute of Technology, Eggenstein-Leopoldshafen, Germany. ⁵These authors contributed equally: Lukas Grünhaupt, Martin Spiecker. *e-mail: ioan.pop@kit.edu

Supplementary Information

Granular aluminum: A superconducting material for high impedance quantum circuits

Lukas Grünhaupt,^{1,*} Martin Spiecker,^{1,*} Daria Gusenkova,¹ Nataliya Maleeva,¹ Sebastian T. Skacel,^{1,2} Ivan Takmakov,^{1,2,3} Francesco Valenti,^{1,4} Patrick Winkel,¹ Hannes Rotzinger,¹ Wolfgang Wernsdorfer,^{1,2} Alexey V. Ustinov,^{1,3} and Ioan M. Pop^{1,2,†}

¹*Physikalisches Institut, Karlsruhe Institute of Technology, 76131 Karlsruhe, Germany*

²*Institute of Nanotechnology, Karlsruhe Institute of Technology, 76344 Eggenstein-Leopoldshafen, Germany*

³*Russian Quantum Center, National University of Science and Technology MISIS, 119049 Moscow, Russia*

⁴*Institute for Data Processing and Electronics, Karlsruhe Institute of Technology, 76344 Eggenstein-Leopoldshafen, Germany*

(Dated: March 13, 2019)

In this supplementary information we provide further information on the sample fabrication, the granular aluminum evaporation, the characteristic impedance of the superinductor, the fluxonium Hamiltonian, the time-domain setup, the measured coherence times at the $\Phi_{\text{ext}} = 0$ sweet spot, and the reproducibility of our results.

SAMPLE FABRICATION: SHADOW EVAPORATION SEQUENCE

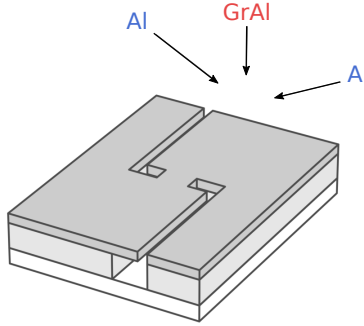


Figure S1. Sketch of the resist stack for structuring the Josephson junction. It combines a Niemeyer-Dolan bridge [1, 2] in its middle with an asymmetric undercut [3] for the feedlines, which are patterned by a double-angle evaporation of pure aluminum. The final zero angle evaporation of grAl does not cover the aluminum film in the vicinity of the Josephson junction and its feedlines. A connection between the junction and the superinductor is ensured by connection pads at the end of the $\sim 2 \mu\text{m}$ long feedlines (not shown, cf. Fig. 1 in the main text).

We fabricated the entire circuit by a three-angle evaporation process using a PMMA/(PMMA-MMA) resist stack on a double-side polished c-plane sapphire substrate. Fig. S1 schematically shows the lithography mask for the Al/AlOx/Al Josephson junction, which is patterned using a 50 keV e -beam writer. The mask combines a Niemeyer-Dolan bridge [1, 2] with an asymmetric undercut [3] for the feedlines. In a first step the Josephson junction is patterned by a two-angle aluminum evaporation process with a thickness of 20 nm and 30 nm, respectively. Thereby, all wires of the design parallel to the evaporation direction, and the antenna, due to its width, are deposited (cf. Fig. 1 in the main text). Finally, without breaking the vacuum, we patterned all inductive parts of the circuit by a zero-angle evaporation of a 40 nm thick grAl film with a resistivity $\rho = 0.8 \times 10^3 \mu\Omega \text{cm}$. The junction and its feedlines (see Fig. S1 and cf. Fig. 1 in the main text) are connected to the grAl film using connection pads $\sim 2 \mu\text{m}$ away from the Josephson junction.

* Both authors contributed equally.

† ioan.pop@kit.edu

SAMPLE FABRICATION: GRANULAR ALUMINUM EVAPORATION

To deposit the grAl film we use a dedicated pure aluminum crucible in a commercial, controlled-angle e -beam evaporation machine (Plassys MEB 550STM). The machine has two chambers, one that is used for oxidation and doubles as loadlock, and a second UHV chamber for metal evaporation. Pure aluminum is evaporated at a rate of 0.3 nm/s while we admit a mass-flow of 1.3 sccm of pure oxygen into the oxidation chamber. Due to the continuous pumping on the chamber we obtain a dynamic oxygen pressure on the order of 2.2×10^{-5} mbar, while the pressure in the evaporation chamber is on the order of 4.5×10^{-6} mbar. The grAl resistivity changes exponentially with the oxygen partial pressure (cf. Ref. [4]). In practice we obtain film resistivities reproducible within a factor of two from one evaporation to the next.

The main steps of our process flow for granular aluminum evaporation are the following:

1. Pump the loadlock for 3 h down to a pressure in the range of 5×10^{-7} mbar,
2. Oxygen plasma cleaning for 2 min [5] (Kaufman source parameters: 120 V acceleration voltage, 10 mA, 10 sccm O₂, 5 sccm Ar, resulting in a PMMA etch rate of about 0.35 nm s^{-1}),
3. Titanium evaporation with closed shutter (0.2 nm s^{-1} for 2 min),
4. Regulate aluminum evaporation rate to 0.3 nm s^{-1} ,
5. Regulate oxygen flow to 1.0 - 1.5 sccm (corresponding to resistivities from 0.2 to $2 \text{ m}\Omega \text{ cm}^2$, depending on the targeted resistivity),
6. Open shutter,
7. Wait for desired grAl film thickness, close shutter, stop oxygen flow, ramp down aluminum evaporation rate,
8. Target rinsing (evaporate 20 nm of pure aluminum at 1 nm s^{-1} with the shutter closed and no oxygen).

CHARACTERISTIC IMPEDANCE OF THE SUPERINDUCTOR

From fitting the measured fluxonium spectrum, we obtain a total superinductance of $L_{\text{total}} = 225.6 \text{ nH}$ and a fluxonium capacitance $C_J = 5.2 \text{ fF}$ (see main text), which leads to a qubit plasmon mode impedance of $Z = 6.6 \text{ k}\Omega$. In order to estimate the impedance of the bare superinductor, we measured the Junction size using a SEM image [cf. Fig. 1e)] in the main text) to be $0.06 \mu\text{m}^2$ with an error of 20%. Using a Josephson junction capacitance per area of $c_J = 50 \text{ fF } \mu\text{m}^{-2}$ we calculate a capacitance of 3 fF for the fluxonium junction alone. This yields a capacitance $C_s = 2.2 \text{ fF}$ associated with the superinductor. Using these values we obtain a superinductor characteristic impedance $Z = \sqrt{L_{\text{total}}/C_s} \approx 10 \text{ k}\Omega$.

For comparison we simulated the superinductor loop, approximating the junction with an ideal capacitor with 3 fF. We obtain a resonant frequency of 5.4 GHz, from which we calculate a superinductor self capacitance of $C'_s = 0.9 \text{ fF}$. Using this method, the superinductor characteristic impedance is estimated to be $Z = 16 \text{ k}\Omega$. In this simulation, we find the next self-resonant mode of the superinductor at 17.4 GHz, well above the qubit spectrum.

FLUXONIUM HAMILTONIAN

The Hamiltonian of the bare fluxonium qubit reads

$$H = \frac{1}{2C} q^2 + \frac{1}{2L} \phi^2 - E_J \cos \left(\frac{2\pi}{\Phi_0} (\phi - \Phi_{\text{ext}}) \right),$$

with ϕ and q being the flux and charge operators obeying the commutation relation $[\phi, q] = i\hbar$. The spectrum of the Hamiltonian can be tuned by varying the external flux Φ_{ext} penetrating through the fluxonium loop.

Following the methodology of Ref. [6] the circuit quantization of the fluxonium qubit inductively coupled to its readout resonator [cf. Fig. 1a)] yields the following system hamiltonian:

$$H = \frac{1}{2} \phi^T \frac{1}{L_r L_q + L_r L_s + L_q L_s} \begin{pmatrix} L_q + L_s & -L_s \\ -L_s & L_r + L_s \end{pmatrix} \phi + \frac{1}{2} \mathbf{q}^T \begin{pmatrix} \frac{1}{C_r} & \\ & \frac{1}{C_q} \end{pmatrix} \mathbf{q} - E_J \cos \left(\frac{2\pi}{\Phi_0} (\phi_q - \Phi_{\text{ext}}) \right),$$

Numerical diagonalization of both Hamiltonians is also performed according to Ref. [6].

FLUXONIUM HAMILTONIAN WITH A SQUID-JUNCTION

In order to be able to tune in-situ the Josephson energy by applying a magnetic field, we also fabricated a sample where the junction is constructed in the shape of a SQUID as shown in Fig. S2. We refer to this sample as fluxonium S. The non-linear term in the Hamiltonian now consists of two junction terms, using $\varphi_i = 2\pi\Phi_i/\Phi_0$ they read

$$\begin{aligned} & E_{J_1} \cos(\varphi - \varphi_l) + E_{J_2} \cos(\varphi - (\varphi_l + \varphi_s)) \\ &= (E_{J_1} + E_{J_2}) \cos\left(\frac{\varphi_s}{2}\right) \cdot \cos\left(\varphi - \varphi_l - \frac{\varphi_s}{2}\right) - (E_{J_1} - E_{J_2}) \sin\left(\frac{\varphi_s}{2}\right) \cdot \sin\left(\varphi - \varphi_l - \frac{\varphi_s}{2}\right) \\ &= E_\Sigma(\varphi_s) \cdot \cos(\varphi - \varphi_{\text{ext}}) - E_\Delta(\varphi_s) \cdot \sin(\varphi - \varphi_{\text{ext}}) \\ &= \text{sgn}[E_\Sigma(\varphi_s)] \cdot \sqrt{E_\Sigma(\varphi_s)^2 + E_\Delta(\varphi_s)^2} \cdot \cos\left(\varphi - \varphi_{\text{ext}} - \arctan\left[\frac{E_\Sigma(\varphi_s)}{E_\Delta(\varphi_s)}\right]\right), \end{aligned}$$

where the effective external flux is defined by $\varphi_{\text{ext}} = \varphi_l + \varphi_s/2$, and the flux dependent effective Josephson energies are $E_\Sigma(\varphi_s) = (E_{J_1} + E_{J_2}) \cos(\varphi_s/2)$ and $E_\Delta(\varphi_s) = (E_{J_1} - E_{J_2}) \sin(\varphi_s/2)$. As expected, the SQUID flux only contributes half. Tuning of E_J is given by the square root term depending on the SQUID flux. Note that there is a phase role-off term inside the cosine, which can directly be seen in the spectrum (see Fig. S2).

If the areas have a ratio of $V = A_l/A_s$, the flux in the SQUID is related to the external flux by

$$\frac{\varphi_s}{2} = \frac{1}{2V+1} \cdot \varphi_{\text{ext}}. \quad (\text{S1})$$

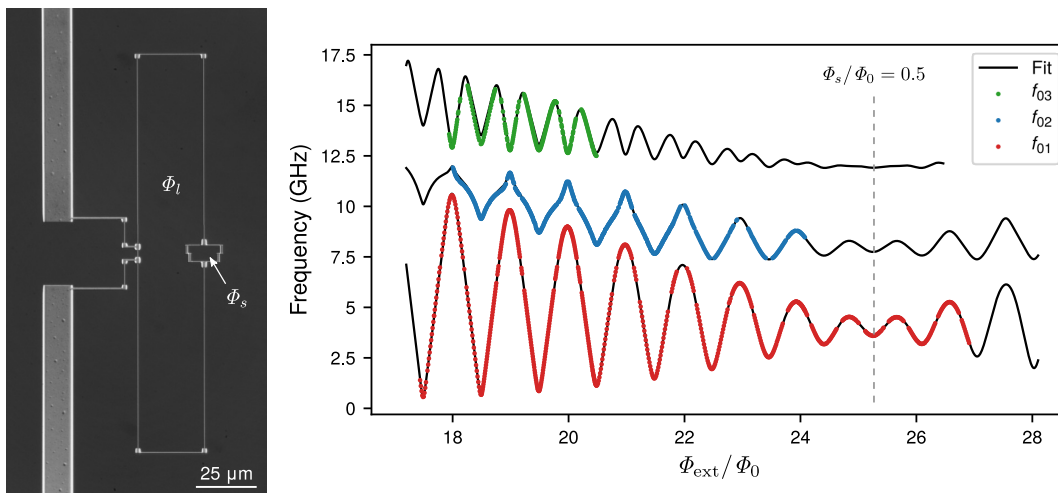


Figure S2. Optical image of fluxonium S and the measured spectrum. Left: Optical image of the fluxonium qubit with a SQUID-junction (cf. Fig. 1). Right: Two-tone spectroscopy close to Φ_s corresponding to full SQUID frustration. From the fit we extract $L = 233.5$ nH, $C = 6.85$ fF, $E_\Sigma(0)/h = 20.1$ GHz, $E_\Delta(\pi)/h = 0.59$ GHz, and the area ratio $V = 50$. The large anharmonicity of the fluxonium qubit is evident from the measured values of the first three transitions of the spectrum.

TIME-DOMAIN SETUP

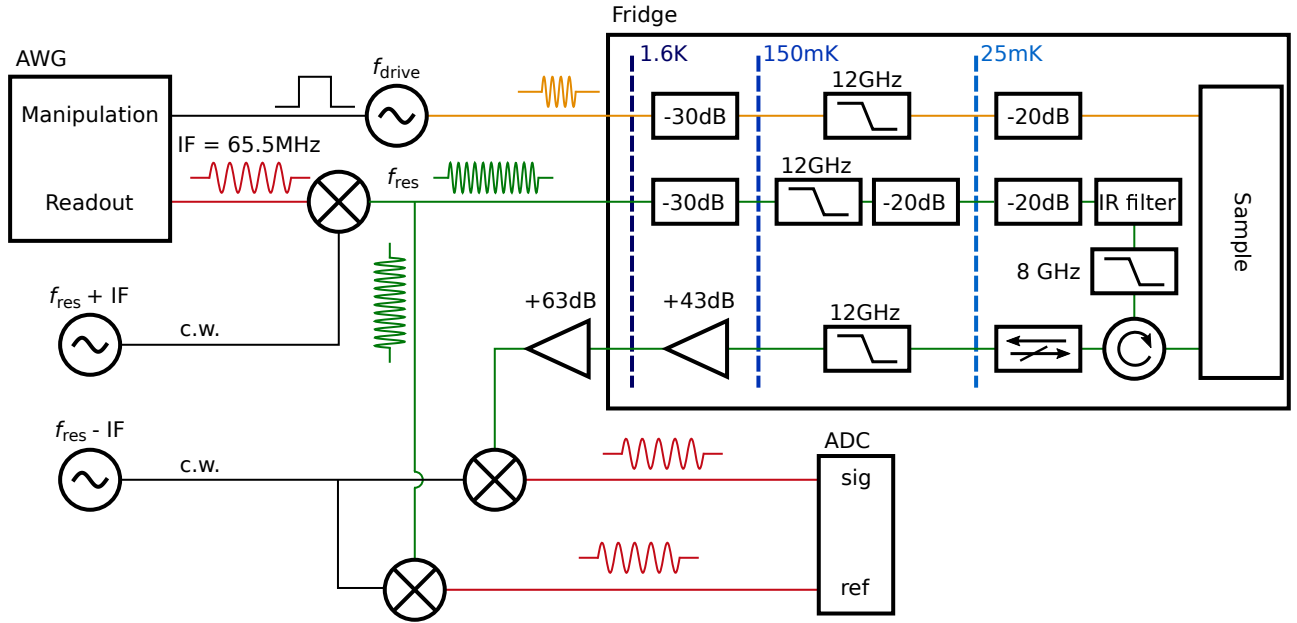


Figure S3. Interferometer setup for time-domain manipulation and measurements. Two separate channels of a commercial arbitrary waveform generator (AWG) provide the pulse shaping abilities for the readout and manipulation pulses. We perform homodyne manipulation by feeding the square envelope pulse from the AWG into the IQ -modulation ports of a commercial microwave generator set to the qubit transition frequency. The readout uses a low-cost commercial two-channel microwave generator operated in continuous wave mode in addition to an AWG channel in an interferometric configuration. First, the readout pulse at an intermediate frequency $IF = 65.5$ MHz is upconverted to the readout frequency and split into two signals. One signal is directly measured with the analog digital converter (ADC), whereas the other signal first passes the fridge. Both signals are interfered computationally to extract the I and Q quadratures. All microwave lines in the cryostat are attenuated and filtered using commercially available components. An additional home-made infrared (IR) filter employing Stycast[®], and designed to have an impedance of $50\ \Omega$ at cryogenic temperatures, ensures an attenuation of more than -10 dB for frequencies larger than 60 GHz.

COHERENCE TIMES OF FLUXONIUM A AT $\Phi_{\text{ext}} = 0$

The dynamic of the T_1 relaxation shown in Fig. S4a) is well described by a sum of two exponential decays. This might be explained by the existence of an additional decay channel, on average present with a probability p_q . The timescale over which this channel influences the energy relaxation needs to be longer than the measurement pulse sequence, which here is $30\ \mu\text{s}$. Thus we average measurements with no additional decay resulting in T_r and traces with an additional decay T_q . We fit the measured T_1 relaxation with

$$P(t) = p_q \cdot e^{-\left(\frac{1}{T_q} + \frac{1}{T_r}\right) \cdot t} + (1-p_q) \cdot e^{-\frac{1}{T_r} \cdot t}. \quad (\text{S2})$$

We attribute this additional decay channel to quasiparticles tunneling across the Josephson junction, similar to [7]. At the $\Phi_{\text{ext}}/\Phi_0 = 0$ sweet spot we measure a coherence time $T_2^* = 3.8\ \mu\text{s}$ using a Ramsey fringes measurement [8], about one order of magnitude shorter than at the $\Phi_{\text{ext}}/\Phi_0 = 0.5$ sweet spot (cf. Fig. 3 in the main text). Figure S4c) shows T_2^* (green squares) and the qubit transition frequency relative to the maximum value of $f_{0,0}^q = 12.538$ GHz (red circles) as a function of the externally applied magnetic flux.

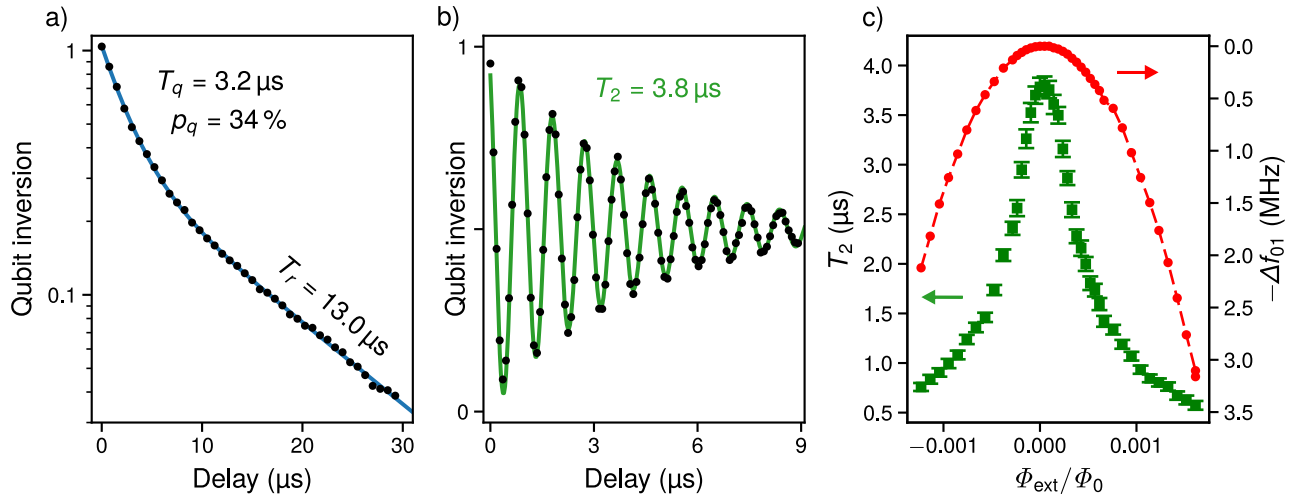


Figure S4. a) Relaxation time T_1 at $\Phi_{\text{ext}} = 0$. The relaxation is well described by a sum of two exponential functions (see Eq. (S2)), assuming time traces with a remaining relaxation time T_r and traces with increased relaxation, at a probability p_q , giving rise to an additional relaxation T_q (measured data - black points, fit - blue solid line) b) The black points show the result of a Ramsey fringes measurement for a 1.15 MHz detuned drive with respect to the qubit frequency of $f_{0,0}^q = 12.538$ GHz at $\Phi_{\text{ext}} = 0$, averaged over 30 min. From the fit of an exponentially decaying cosine (green solid line) we extract a coherence time $T_2^* = 3.8 \mu\text{s}$. c) Flux dependence of the coherence time T_2^* (green squares) and the measured qubit detuning (red points) with respect to $f_{0,0}^q$ close to zero flux. The red dashed line connecting the points is a guide to the eye.

SPECTROSCOPY OF FLUXONIUM SAMPLE A AND B AFTER THERMAL CYCLING

In Fig. S5 we show the measured qubit spectrum for fluxonium A and B, which were fabricated in the same batch. For fluxonium A, compared to the data presented in the main text (cf. Fig. 2), the spectrum in Fig. S5 was measured after thermal cycling twice to room temperature and a total storage time of six weeks in ambient atmosphere.

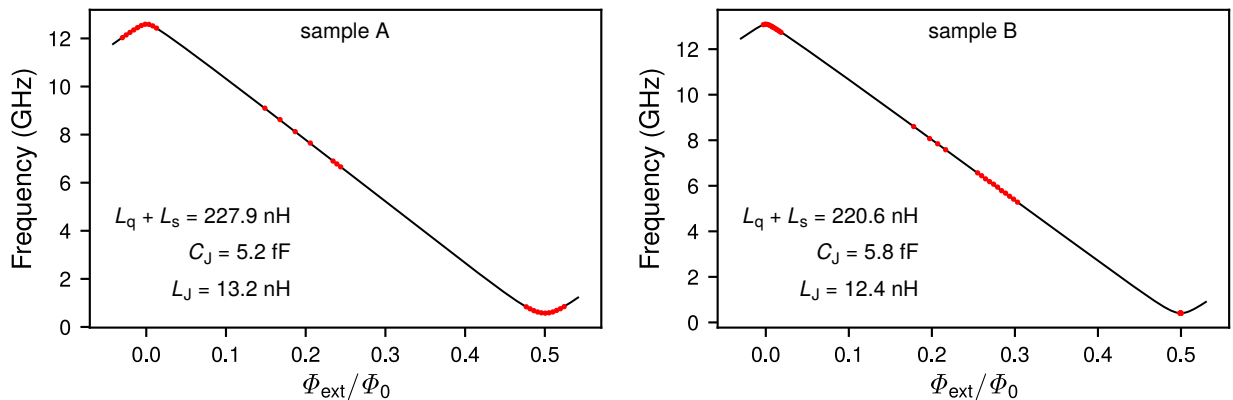


Figure S5. Measured spectrum of fluxonium sample A (left) and B (right), fabricated in the same batch. The black lines show a numerical fit of the Hamiltonian. The fit parameters are listed in the corresponding panel. For sample A the maximum and minimum frequencies are 12.589 GHz and 575 MHz, for sample B they are 13.093 GHz and 406 MHz.

COHERENCE MEASUREMENTS ON FLUXONIUM SAMPLE B

Figure S6 shows coherence measurements on fluxonium sample B performed at the two flux sweet spots.

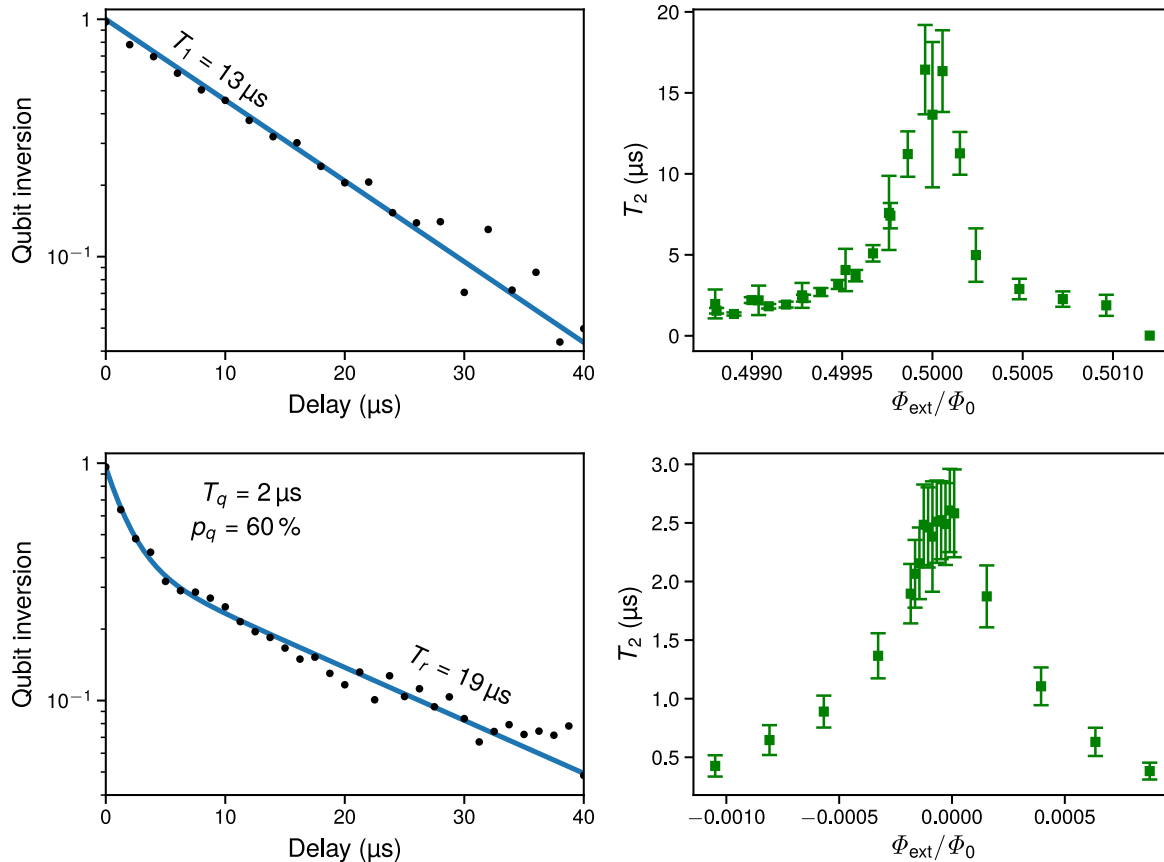


Figure S6. Coherence measurements on fluxonium sample B at the $\Phi_{\text{ext}}/\Phi_0 = 0.5$ (top) and $\Phi_{\text{ext}}/\Phi_0 = 0$ (bottom) sweet spot. Energy relaxation measurements are shown in the left panels. The double-exponential decay visible at $\Phi_{\text{ext}}/\Phi_0 = 0$ is consistent with the measurements in sample A [cf. Fig. S4a)] and similar to previous results in Ref. [7] and Ref [9].

-
- [1] J. Niemeyer, PTB-Mitteilungen **84**, 251 (1974).
 - [2] G. J. Dolan, Appl. Phys. Lett. **31**, 337 (1977).
 - [3] F. Lecocq, I. M. Pop, Z. Peng, I. Matei, T. Crozes, T. Fournier, C. Naud, W. Guichard, and O. Buisson, Nanotechnology **22**, 315302 (2011).
 - [4] H. Rotzinger, S. T. Skacel, M. Pfirrmann, J. N. Voss, J. Münzberg, S. Probst, P. Bushev, M. P. Weides, A. V. Ustinov, and J. E. Mooij, Supercond. Sci. Technol. **30**, 25002 (2017).
 - [5] I. M. Pop, T. Fournier, T. Crozes, F. Lecocq, I. Matei, B. Pannetier, O. Buisson, and W. Guichard, J. Vac. Sci. Technol. B **30**, 10607 (2012).
 - [6] W. C. Smith, A. Kou, U. Vool, I. M. Pop, L. Frunzio, R. J. Schoelkopf, and M. H. Devoret, Phys. Rev. B **94**, 144507 (2016).
 - [7] I. M. Pop, K. Geerlings, G. Catelani, R. J. Schoelkopf, L. I. Glazman, and M. H. Devoret, Nature **508**, 369 (2014).
 - [8] N. F. Ramsey, Phys. Rev. **78**, 695 (1950).
 - [9] S. Gustavsson, F. Yan, G. Catelani, J. Bylander, A. Kamal, J. Birenbaum, D. Hover, D. Rosenberg, G. Samach, A. P. Sears, S. J. Weber, J. L. Yoder, J. Clarke, A. J. Kerman, F. Yoshihara, Y. Nakamura, T. P. Orlando, and W. D. Oliver, Science **354**, 1573 (2016).